ACS APPLIED MATERIALS & INTERFACES

Research Article

www.acsami.org

A Cu^{2+} ion−F Center Complex View on the Photoluminescence Quenching and Correlating Ferrimagnetism in $(Cu_2^{+}/Cu_1^{2+})_{0.044}Zn_{0.956}O$ Electrospun Nanobelts

Jian-Min Li,*[,†] Xian-Lin Zeng,[†] Dan-Ping Wei,[†] Yun-Bing Hu,[†] and Zhu-An Xu[†,‡]

[†]Department of Physics and [‡]State Key Laboratory of Silicon Materials, Zhejiang University, Hangzhou 310027, People's Republic of China

ABSTRACT: Unlike to the most previous reports, mixed-cation Cu^{+}/Cu^{2+} doping-induced novel nanoscale phenomena, including photoluminescence quenching and a correlating ferrimagnetism with Néel temperature ≈ 14 K, were found in the as-calcined $(Cu_2^{+}/Cu_1^{2+})_{0.044}Zn_{0.956}O$ electrospun nanobelts (NBs). There is also high strain (up to 1.98%) and shrunk lattice distortion ($\Delta V/V_0 \sim 0.127\%$) in the $(Cu_2^{+}/Cu_1^{2+})_{0.044}Zn_{0.956}O$ NBs, leading to broken lattice symmetry in conjunction with nonstoichiometry (i.e., oxygen vacancies or accurate F centers), which could be possible origins of ferrimagnetism in the Cu-doped ZnO NBs. Electron paramagnetic resonance spectra reveal that there are giant and anisotropic g factors, suggesting that there is strong anisotropic spin−orbit interaction between the Cu^{2+} ion and F center (i.e., forming Cu^{2+}−F^{+} complexes) in the $(Cu_2^{+}/Cu_1^{2+})_{0.044}Zn_{0.956}O$ NBs. The above correlation enables the potential application of tuning of the optical and ferrimagnetic properties through strain and F-center engineering.

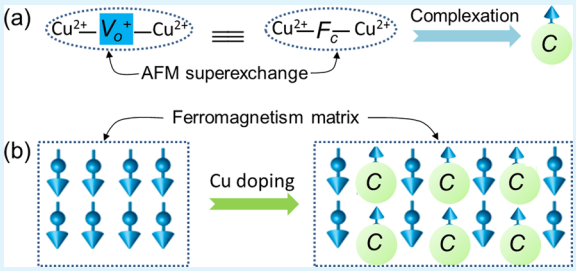

KEYWORDS: *diluted magnetic semiconducting oxides, $(Cu_2^{+}/Cu_1^{2+})_{0.044}Zn_{0.956}O$ electrospun nanobelts, photoluminescence quenching, Cu^{2+} ion−F center complexes*

1. INTRODUCTION

Semiconductor nanowires (NWs) often exhibit novel electronic and optical properties because of their unique one-dimensional (1D) structure and quantum confinement effects, among which 1D nanostructure-based diluted magnetic semiconducting oxides (DMSOs) are very important for nanoscale spintroncs.[1,2] Thanks to excellent doping uniformity and result reproducibility, the solution-based electrospinning synthetic strategy is believed to be a universal and versatile method for fabricating 1D nanofibers with diameters ranging from tens of nanometers to several micrometers.[3,4] Our recent works successfully prepared some complex oxide nanofibers using a poly(vinyl alcohol) (PVA) electrospinning technique with a subsequent calcination approach.[5−9] On the other hand, generally, chemical doping with 3d transition-metal (3d-TM cationic) atoms (such as Fe, Co, Ni, and Mn having permanent magnetic moments) is a well-known frequently used route to enable their diluted magnetism of semiconductors; however, the origin and control of the magnetism in the 3d-TM-doped DMSOs, such as zinc oxide (ZnO), is far from well understood.[10,11] Cu is a traditional nonmagnetic element; however, Cu^{2+} ($3d^9$) ion is ferromagnetic [$S = {}^1/_2$; $\mu(Cu^{2+}) \sim 1.9\ \mu_B$], while Cu^{+} ($3d^{10}$) has a fully occupied 3d shell and hence does not contribute to ferromagnetism [$S = 0$; $\mu(Cu^{+}) \sim 0$].[12]

On the other hand, the Cu ion is an active luminescent center, and its emission is sensitive to the atomic environment, such as the doping concentration and defects in the host.[13] For example, broad and continuous photoluminescence (PL) spectra were observed in Cu-doped ZnO NWs.[14] Recently, green luminescence was observed in Cu-doped ZnO thin films[15] and Cu-doped ZnO nanorods.[16] Green emission is commonly observed in ZnO nanostructures, and surface states are responsible for the green emission.[17,18] However, some different hypotheses have been proposed that bulk defects such as oxygen vacancies (V_O) are also responsible for the green emission.[19−22] The presence of V_O is proven to have a great effect on other electronic properties of ZnO. Chakraborti et al. first reported room temperature ferromagnetism (RTFM) in $Zn_{1-x}Cu_xO$ thin films.[23] Subsequently, robust RTFM was observed in Cu-doped ZnO thin films.[24] An interesting question thus arises: Is there any correlation between PL and their diluted magnetism of semiconductors, and further can we tune the optical and magnetic properties of ZnO nanocrystals through V_O engineering? Here, we report the synthesis of the Cu-doped ZnO ($Cu_{4.4}Zn_{95.6}O$, atom %, or $(Cu_2^{+}/Cu_1^{2+})_{0.044}Zn_{0.956}O$) beltlike nanostructures or nanobelts (NBs) by electrospinning and subsequent calcination. The $(Cu_2^{+}/Cu_1^{2+})_{0.044}Zn_{0.956}O$ electrospun NBs were 1D nanostructures, with about 80−90 nm thickness, 180−300 nm width, and length up to several hundreds of micrometers. Novel phenomena, including PL quenching and correlating ferrimag-

Received: January 14, 2014
Accepted: March 6, 2014
Published: March 6, 2014

   dx.doi.org/10.1021/am5001135 | *ACS Appl. Mater. Interfaces* 2014, 6, 4490−4497

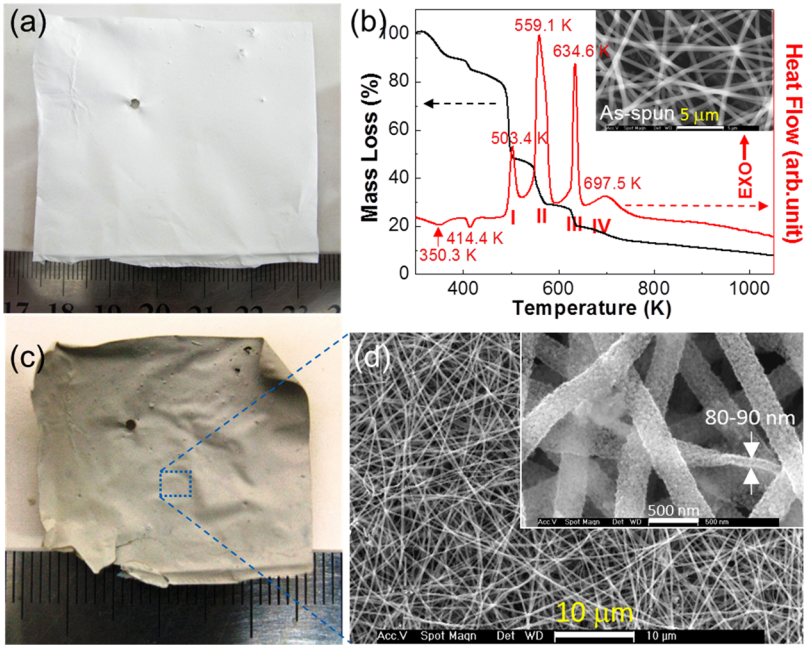

Figure 1. (a) Digital photograph of the gray-white as-electrospun PVA/$(Cu_2^+/Cu_1^{2+})_{0.044}Zn_{0.956}O$ composite fiber mats. (b) DSC–TGA (TA, SDT Q600) curves of the as-electrospun PVA/$(Cu_2^+/Cu_1^{2+})_{0.044}Zn_{0.956}O$ composite fibers. The heating rate is at 10 K min^{-1} under a static ambient atmosphere. Inset: Low-magnification SEM images of the as-electrospun $(Cu_2^+/Cu_1^{2+})_{0.044}Zn_{0.956}O$ fibers. (c) Digital photograph of the greenish as-calcined $(Cu_2^+/Cu_1^{2+})_{0.044}Zn_{0.956}O$ NB mats. (d) Typical SEM image of the as-calcined $(Cu_2^+/Cu_1^{2+})_{0.044}Zn_{0.956}O$ NBs. Inset: SEM image with higher magnification.

netism, were observed in the $(Cu_2^+/Cu_1^{2+})_{0.044}Zn_{0.956}O$ NBs, which was different from the above reports.[14−16,23,24] There is high strain (up to 1.98%) and shrunken lattice distortion ($\Delta V/V_0 \sim 0.127\%$) in the $(Cu_2^+/Cu_1^{2+})_{0.044}Zn_{0.956}O$ NBs, leading to broken lattice symmetry [confirmed by powder X-ray diffraction (PXRD)] and nonstoichiometry (i.e., V_O confirmed by X-ray photoemission), which were proposed as possible origins of ferrimagnetism. The correlation in the Cu-doped ZnO NBs enables the potential applications of tuning of the optical properties and ferrimagnetism of ZnO-based DMSO NWs through strain and V_O engineering.

2. EXPERIMENTAL SECTION

$(Cu_2^+/Cu_1^{2+})_{0.044}Zn_{0.956}O$ NBs have been fabricated by the electrospinning technique, and the chemicals were commercially available (Sinopharm Chemical Reagent Company) and were used as received without further purification. For a typical procedure, 2.8 g of poly(vinyl alcohol) (PVA1788; M_w = ca. 66000 or 996 kg mol^{-1}) powder was dissolved in 18 mL of deionized water in one vial, and after stirring at 343 K for 1 h, a viscous colorless solution of PVA was obtained. Meanwhile, predetermined amounts of 2.3995 g of zinc acetate [$Zn(Ac)_2{\cdot}2H_2O$, purity of 99.99%] powder and 0.1005 g of copper acetate [$Cu(Ac)_2{\cdot}H_2O$, purity of 99.999%] powder were dissolved with 5 mL of deionized water in another separate vial (brown red color) and slowly added to the PVA solution at a rate of 1 drop s^{-1} with constant stirring at 343 K for 3 h. The light-blue buffer solution was maintained at 298 K for 5 h with magnetic stirring and then left for more than 15 h to ensure complete dissolution and elimination of the air bubbles. Electrospinning was then undertaken using a homemade vertical needle-collector setup,[5−9] employing the following conditions: controlled flow rate at ∼0.10 mL h^{-1}, applied voltage ∼11.0 kV, and tip–collector distance ∼16 cm. The optimal calcination conditions for electrospun nanofibers were found via a four-step process in sequence (a first sintering of the as-electrospun PVA-containing composite fibers at a heating rate of 3 K min^{-1} in an air atmosphere to 503 K for holding 1 h and subsequent cooling to ambient temperature, a second sintering to 559 K for 1 h at the same heating rate and natural cooling, a third sintering to 635 K for 1 h at the same heating rate and natural cooling, a fourth sintering to 698 K for 1 h at the same heating rate and natural cooling, and a fifth sintering to 873 K for 1 h at the same heating rate and natural cooling), yielding the $(Cu_2^+/Cu_1^{2+})_{0.044}Zn_{0.956}O$ single phase of the as-calcined NBs.

3. RESULTS AND DISCUSSION

Figure 1b shows the differential scanning calorimetry (DSC)–thermogravimetric analysis (TGA) curves of the as-electrospun PVA-containing composite fibers. There are two endothermic peaks at 350.3 and 414.4 K, respectively, that can be attributed to crystal water loss. Also, four exothermic peaks in the DSC curve are observed at 503.4, 559.1, 634.6, and 697.5 K, respectively. The first three sharp exothermic peaks are responsible for the onset of PVA decomposition, and the fourth weak peak is crystallization of $(Cu_2^+/Cu_1^{2+})_{0.044}Zn_{0.956}O$, concurrent with a significant weight loss of about ∼92.4 wt % taking place, indicating the complete removal of the organic component. The inset of Figure 1b shows that the as-electrospun PVA-containing composite fibers were 1D nanostructures, with a mean fiber diameter of approximately 300–400 nm and a length of several hundreds of micrometers. Following the above four-step calcination, it was found that the color of the Cu-doped ZnO fiber mats turned from gray-white (Figure 1a) to greenish (Figure 1c). Figure 1d shows the scanning electron microscopy (SEM) image of the as-calcined $(Cu_2^+/Cu_1^{2+})_{0.044}Zn_{0.956}O$ NBs, having a length of up to several hundreds of micrometers by this simple approach. A close-up SEM image clearly reveals that the $(Cu_2^+/Cu_1^{2+})_{0.044}Zn_{0.956}O$ nanofibers are beltlike nanostructures with thickness of approximately 80–90 nm and width of approximately 180–300 nm (Figure 1d).

Representative transmission electron microscopy (TEM; Figure 2a) of the as-calcined electrospun sample reveals that

dx.doi.org/10.1021/am5001135 | ACS Appl. Mater. Interfaces 2014, 6, 4490–4497

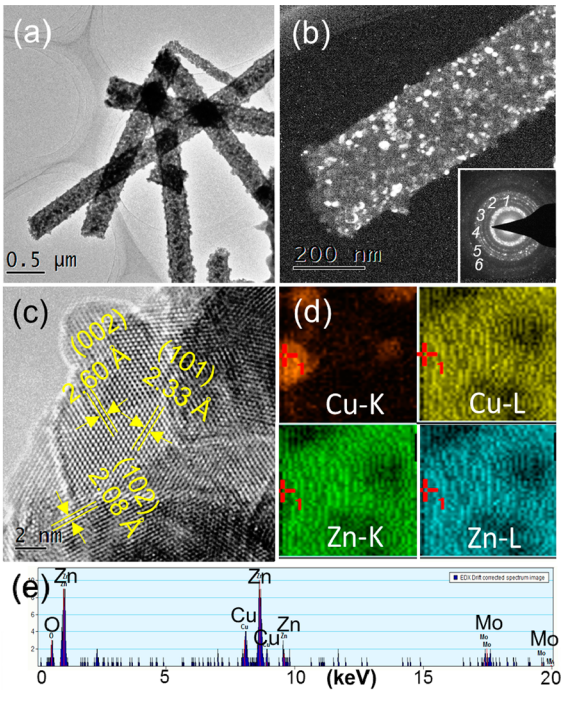

Figure 2. (a) Typical bright-field and (b) dark-field TEM images of the as-calcined $(Cu_2^+/Cu_1^{2+})_{0.044}Zn_{0.956}O$ NBs, showing tiny nanograins. Inset in part b: SAED pattern indicating a nanoscale polycrystalline structure. Numbers on the ring pattern correspond to the 100 (1), 101 or 110 (2), 002 (3), 102 or 201 (4), 112 (5), and 103 (6) planes. (c) HRTEM (FEI TECNAI G^2 F20, 200 kV) image of the as-calcined $(Cu_2^+/Cu_1^{2+})_{0.044}Zn_{0.956}O$ NBs. (d) EDX mappings of Cu (upper left and right) and Zn (lower left and right). (e) Typical EDX spectrum of a single $(Cu_2^+/Cu_1^{2+})_{0.044}Zn_{0.956}O$ NB. Peaks corresponding to Zn, O, and Cu are evident. Mo signals are from a Mo TEM grid supporting the NWs. The specimens for HRTEM analysis were prepared by dissolving the black powder in ethanol. After ultrasonic treatment, a drop of the liquid was sprayed onto a holey-C Mo grid in order to avoid confusion with the Cu dopant.

the $(Cu_2^+/Cu_1^{2+})_{0.044}Zn_{0.956}O$ NBs have a beltlike structure with uniform diameter and thickness. A closer dark-field TEM image (Figure 2b) of the as-calcined $Cu_{4.4}Zn_{95.6}O$ NBs shows a grain size of approximately 25−40 nm. The inset in Figure 2b shows the corresponding selected-area electron diffraction (SAED) pattern. The continuous sharp rings further confirm that the $(Cu_2^+/Cu_1^{2+})_{0.044}Zn_{0.956}O$ NBs are constituted of many very tiny nanocrystals. The representative high-resolution TEM (HRTEM) images indicated that the $(Cu_2^+/Cu_1^{2+})_{0.044}Zn_{0.956}O$ NBs are made of many randomly oriented nanoscale polycrystals (Figure 2c). As shown in Figure 2d, the TEM−energy-dispersive X-ray spectrometry (EDX) elemental mappings of Cu and Zn vividly prove the existence and homogeneous distribution of Cu. TEM−EDX measurements prove that the ratio of Cu/(Cu + Zn) is 0.045:1, approaching the nominal value of 0.044:1 (Figure 2e).

The phase composition and structure of the as-calcined products were examined by PXRD. As shown in Figure 3a, no other secondary phases are observed, and all of the strong reflection peaks from the as-calcined electrospun $(Cu_2^+/Cu_1^{2+})_{0.044}Zn_{0.956}O$ NBs can be readily indexed to hexagonal wurtzite-structured ZnO (JCPDS 36-1451), revealing the successful incorporation of Cu into the host ZnO lattice. All PXRD data are fitted by Rietveld refinement using the *RIETAN 2000* program.[25] From the PXRD refinement results, the lattice parameters (a = 3.2493 Å and c = 5.2059 Å) of the $(Cu_2^+/Cu_1^{2+})_{0.044}Zn_{0.956}O$ NBs are slightly smaller than that of bulk ZnO (a = 3.2500 Å and c = 5.2070 Å), suggesting a shrunken lattice structure ($\Delta V/V_0 \sim 0.127\%$) in the $(Cu_2^+/Cu_1^{2+})_{0.44}Zn_{0.956}O$ NBs, while the corresponding bulk values and consequent lattice distortion are very small,[26] which is consistent with the case of Al_2O_3 nanocrystals.[27] Furthermore, according to the Williamson−Hall method,[28,29] with the (100), (002), and (101) peaks, if the broadening functions are of the Cauchy type, there is a relatively high internal strain (1.98%) in the $(Cu_2^+/Cu_1^{2+})_{0.044}Zn_{0.956}O$ NBs with an average crystallite size of d_{XRD} = 32 nm (Figure 3b), which is compared to the particle size estimated from the TEM dark-field image (Figure 2a).

Figure 3c shows the micro-Raman scattering spectrum of the $(Cu_2^+/Cu_1^{2+})_{0.044}Zn_{0.956}O$ NBs. There are seven distinct visible Raman-active phonon peaks from the $(Cu_2^+/Cu_1^{2+})_{0.044}Zn_{0.956}O$ NBs, which are at 292, 331, 436, 582, 623, 999, and 1125 cm^{-1}. The intense E_2 mode (at ~436 cm^{-1}) was observed, which confirms a typical wurtzite structure.[30] The $E_2 - E_1$ mode at 331 cm^{-1}, the TA + LO mode at 623 cm^{-1}, and two LO modes at 999 and 1125 cm^{-1} can be attributed to the second-order vibration modes of the ZnO wurtzite structure[31] and the structures of group II−IV semiconductors,[32] respectively. On the other hand, ZnO is known as an n-type semiconductor, with V_O acting as the donors, and E_1(LO) at 582 cm^{-1} is always associated with V_O.[33] A new Raman phonon, centered at 292 cm^{-1} (the red question mark guides the eyes), was first observed in the $(Cu_2^+/Cu_1^{2+})_{0.044}Zn_{0.956}O$ NBs with respect to the pure ZnO systems including ZnO microtetrapod-on-NW hybrids,[34] ZnO micro-nanocrystal tetrapods.[35] In our case, upon substitution of Zn with smaller size Cu in the Cu-doped ZnO wurtzite crystal structure, shrinking along c axis occurs in the $Cu_{0.044}Zn_{0.956}O_4$ tetrahedron (inset, top right corner in Figure 3c). The Raman peak at 292 cm^{-1} may result in broken symmetry; e.g., shrunken lattice distortion ($\Delta V/V_0 \sim 0.127\%$; previously confirmed by the above-mentioned PXRD; Figure 3b) in the $(Cu_2^+/Cu_1^{2+})_{0.044}Zn_{0.956}O$ NBs. Another possibility is related to the existence of V_O because the removal of one O atom from the CuO_4 tetrahedron, i.e., by creation of an O vacancy, results in the breaking of one Cu−O bond within the CuO_4 tetrahedron (see the following).

Moreover, the room-temperature PL spectrum of the undoped ZnO NWs (Figure 3d) shows a strong near-band-edge emission at 381 nm (3.25 eV) in the UV and a visible emission at 500 nm (2.48 eV), which is attributed to V_O.[19] In contrast, it was found that no laser spot is visible in the $(Cu_2^+/Cu_1^{2+})_{0.044}Zn_{0.956}O$ NBs (Figure 3d), suggesting that the resulting PL spectra are completely quenched. It is quite different from the large, but thin, transparent ZnO (0001) nanohexagons[36] and extralarge-area flexible ZnO $(01\bar{1}0)$ paperlike nanostructures.[37] This observation was confirmed by the digital images of the pure ZnO NWs, and the $(Cu_2^+/Cu_1^{2+})_{0.044}Zn_{0.956}O$ NBs subjected to laser irradiation showed that no reflection spot was observed (insets, top and bottom in Figure 3d). The PL quenching phenomenon in the $(Cu_2^+/Cu_1^{2+})_{0.044}Zn_{0.956}O$ NBs is different from the case of Au-decorated ZnO nanorods.[38]

Figure 4 shows the magnetization (M−H) loops of the $(Cu_2^+/Cu_1^{2+})_{0.044}Zn_{0.956}O$ NBs measured at room temperature (300 K) and 10 K. A room temperature hysteresis loop is obviously observed in the $(Cu_2^+/Cu_1^{2+})_{0.044}Zn_{0.956}O$ NBs,

dx.doi.org/10.1021/am5001135 | ACS Appl. Mater. Interfaces 2014, 6, 4490−4497

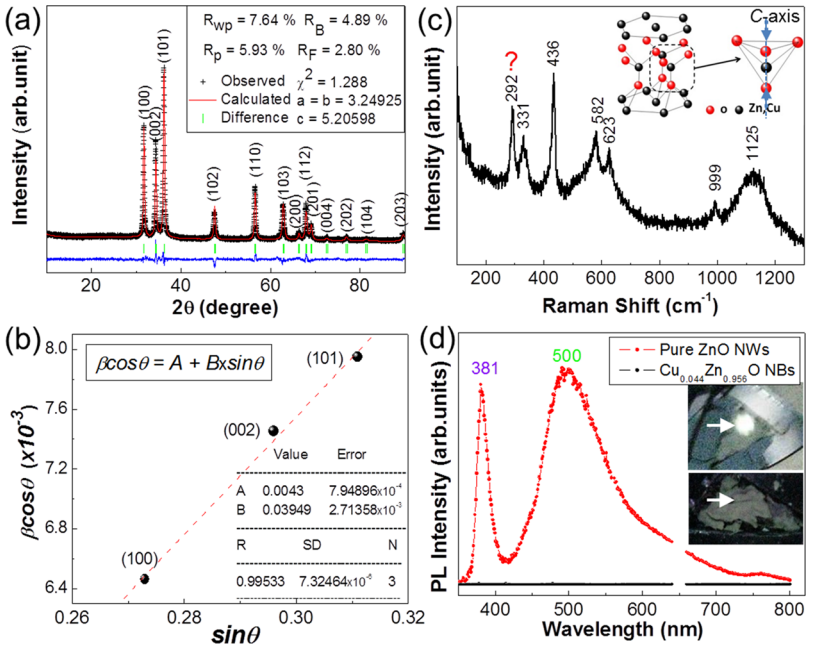

Figure 3. (a) PXRD (The PANalytical Empyrean Series 2 diffraction system) data on a logarithmic scale for the *y* axis of the as-calcined $(Cu_2^+/Cu_1^{2+})_{0.044}Zn_{0.956}O$ NBs and (b) Williamson–Hall plot of the as-calcined $(Cu_2^+/Cu_1^{2+})_{0.044}Zn_{0.956}O$ NBs. (c) Raman spectrum [Jobin Yvon HR-800 spectrometer (resolution of 1 cm^{-1})] of the as-calcined $(Cu_2^+/Cu_1^{2+})_{0.044}Zn_{0.956}O$ NBs. The experiments were carried out in a micro-Raman 180° backscattering geometry with 514.5 nm radiation from a 5 mW argon-ion laser at room temperature. The peak fittings were fit using an 80% Lorentzian–20% Guassian function. (d) Room temperature PL spectrum of the as-calcined $(Cu_2^+/Cu_1^{2+})_{0.044}Zn_{0.956}O$ NBs. The excitation wavelength is 325 nm from a helium–cadmium laser. Insets: digital photographs of the pure as-calcined ZnO NWs (top) and the as-calcined $(Cu_2^+/Cu_1^{2+})_{0.044}Zn_{0.956}O$ NBs (bottom) subjected to laser UV irradiation. The white arrows guide the eyes, and the white spot is the laser spot.

supporting the observation of weak magnetism with the room temperature coercivity (H_c) of 54.5 Oe. The saturation magnetization (M_s) has been estimated to be 5 and 80.5 emu g^{-1} at 300 and 10 K, respectively, by extrapolating *M* versus 1/*H* for 1/*H* tending to zero (not shown here). Furthermore, field cooling (FC) and zero-field cooling (ZFC) were used to clarify and understand the temperature-dependent magnetization in an applied field of 1000 Oe. As the temperature rises, the ZFC magnetization increases first and then decreases after reaching a maximum at 58.5 K (blue arrow), and this is responsible for the lower average blocking temperature (T_B = 58.5 K) of these $(Cu_2^+/Cu_1^{2+})_{0.044}Zn_{0.956}O$ nanograins, suggesting that there are tiny ferromagnetic nanoclusters.[39]

Considering that mixed Cu^+/Cu^{2+} (later confirmed by XPS; Figure 4c) is in the $3d^{10}/3d^9$ mixed-electron configuration, the contribution of magnetic moments is simply from Cu^{2+} [$\mu(Cu^+) \sim 0$],[12] and the saturation magnetization per formula unit (f.u.) was calculated as a function of $\mu(Cu^{2+})$. The net magnetic moment per Cu for the $(Cu_2^+/Cu_1^{2+})_{0.044}Zn_{0.956}O$ NBs is 0.92898 (Table 1), less than the theoretical value of 1.0 μ_B/Cu atom[40] for Cu^{2+} because Cu exhibits a mixed-valence state of Cu^+ and Cu^{2+}. As shown in Table 1, the Curie–Weiss fit $\chi = C/(T - T_\theta)$ of high-temperature magnetization data (green regions, Figure 4b) yields the Curie constant (C) value and Curie–Weiss temperature (T_θ) value. In the case of pure pristine ZnO NWs, a positive T_θ corresponds to ferromagnetism, and a negative T_θ (i.e., the Néel temperature, T_N) corresponds to ferrimagnetism,[41] suggesting that some of the Cu^{2+} ions are in antiferromagnetic (AFM) clusters.[42] Moreover, in contrast to pure ZnO NWs,[6] upon Cu doping, in which T_θ rapidly changes the plus or minus sign to T_N ($-T_\theta \sim 14$ K), the $(Cu_2^+/Cu_1^{2+})_{0.044}Zn_{0.956}O$ NB sample exhibits ferrimagnetic ordering, suggesting that ferromagnetic coupling between the local moments of the ZnO NWs is not robust. Namely, Cu doping into the ZnO wurtzite lattice or substitution of Cu for Zn sites causes tuning in the electronic state, i.e., ferrimagnetic ordering.

Parts c–e of Figure 4 show the results of XPS measurements on our $(Cu_2^+/Cu_1^{2+})_{0.044}Zn_{0.956}O$ NBs. In all of our spectra, the Cu 2p and O 1s peak fittings were fitted using pure Guassian functions. The background (dashed blue lines) was removed by the standard Shirley subtraction method.[43] All of the Cu $2p_{3/2}$ and Cu $2p_{1/2}$ valence band spectra show a shakeup satellite structure (Figure 4c). The Cu $2p_{3/2}$ valence band spectrum at 932.4 eV indicates Cu^+.[44] The Cu $2p_{3/2}$ valence band spectrum at 933.0 eV indicates Cu^{2+}.[45] The Cu $2p_{3/2}$ valence band spectrum at 946 eV indicates Cu^+.[44] The Cu $2p_{3/2}$ valence band spectrum at 952.7 eV indicates Cu^{2+}.[46] Thus, the chemistry of Cu in the $(Cu_2^+/Cu_1^{2+})_{0.044}Zn_{0.956}O$ NBs is conclusively mixed states of Cu^+ and Cu^{2+} ions, and the formation of a Cu metal cluster in our samples can be ruled out. On the basis of the intensity of the Cu $2p_{3/2}$ line, the composition ratio between the Cu^+ and Cu^{2+} ions is estimated to be 2:1. Accordingly, the 4.4% Cu-doped ZnO NBs could be rewritten in the $(Cu_2^+/Cu_1^{2+})_{0.044}Zn_{0.956}O$ NBs. In addition, as shown in Figure 4e, the O 1s peak fittings were fitted using two individual subpeaks at 531.1 eV (the green arrow guides the eyes) and 528.2 eV, respectively. The recent work demonstrates that O 1s at 531.1 eV is considered as evidence of V_O existence.[7,47] Thus, both the high-resolution TEM and XPS measurements suggest that Cu atoms have substituted into the ZnO lattice sites with the existence of some V_O. Combined with the PL spectrum (Figure 3d), it is conclusive that Cu doping drastically limited or forbid the generation and transportation of excitons (i.e., exciton quenching), suggesting that numerous trapped-type defects exist in the $(Cu_2^+/Cu_1^{2+})_{0.044}Zn_{0.956}O$ NBs, and these trapped-

dx.doi.org/10.1021/am5001135 | ACS Appl. Mater. Interfaces 2014, 6, 4490–4497

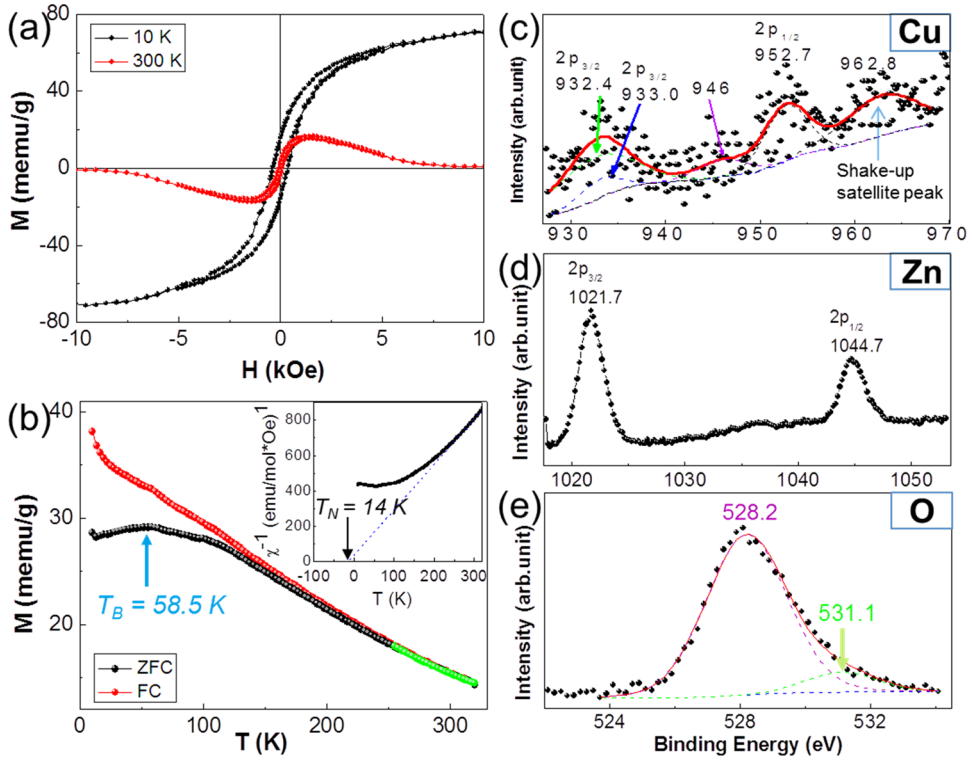

Figure 4. (a) Magnetization loops of the as-calcined $(Cu_2^{+}/Cu_1^{2+})_{0.044}Zn_{0.956}O$ NBs at 10 and 300 K. (b) Temperature-dependent magnetization ($M-T$) curves of the $(Cu_2^{+}/Cu_1^{2+})_{0.044}Zn_{0.956}O$ NBs at a magnetic field of 1000 Oe. ZFC and FC are represented by open red and open black symbols, respectively. The insets are the reciprocal magnetic susceptibilities ($1/\chi$) versus T of the as-calcined $(Cu_2^{+}/Cu_1^{2+})_{0.044}Zn_{0.956}O$ NBs (ZFC mode). The extrapolated straight blue dashed lines of high-temperature data intersecting the temperature axis indicate Curie temperatures using the linear regions (open green symbols). The dark arrow in the inset of b represents T_θ. All magnetic measurements were performed using a Quantum Design MPMS XL-5 superconducting quantum interference device SQUID magnetometer. (c) Cu 2p core-level, (d) Zn 2p core-level, and (e) O 1s core-level XPS spectra in the as-calcined $(Cu_2^{+}/Cu_1^{2+})_{0.044}Zn_{0.956}O$ NBs. The dotted lines guide the eyes. The XPS measurements were performed using a VG ESCALAB MARK II system with a monochromatic Mg Kα X-ray source (1253.6 eV photons; background vacuum of 7.9×10^{-8} Pa).

Table 1. Results of Curie–Weiss Analysis for the Magnetization Curves of the $(Cu_2^{+}/Cu_1^{2+})_{0.044}Zn_{0.956}O$ NBs[a]

			μ_{eff}			
sample	M_s (memu g^{-1}) at 300 K (10 K)	H_c (Oe) at 300 K (10 K)	μ_B/f.u.	μ_B/Cu	T_θ (K)	r_{confid}
$(Cu_2^{+}/Cu_1^{2+})_{0.044}Zn_{0.956}O$	5.0 (80.5)	54.5 (373.0)	1.76506	0.92898	−14.4	0.99784

The effective magnetization value is given in Bohr magnetons per one Cu^{2+} ion in $(Cu_2^{+}/Cu_1^{2+})_{0.044}Zn_{0.956}O$. [a]The linearity fitting in $1/\chi$ versus T curve yields a parameter (effective moment μ_{eff}) with reliability r_{confid}.

type defects (e.g., vacancies) can capture available e^-, neutralizing and forming F centers (F_c).[48] Electrons tend to absorb visible light such that the material looks green in color, which is confirmed by Figure 1c. Therefore, the origin of PL quenching in the $(Cu_2^{+}/Cu_1^{2+})_{0.044}Zn_{0.956}O$ NBs is mainly related to V_O instead of Zn vacancy.[49]

Electron paramagnetic resonance (EPR) spectroscopy is the most powerful experimental technique for identifying and studying the defects that contain unpaired electrons in semiconductors.[50] Variable-temperature EPR spectra of the $(Cu_2^{+}/Cu_1^{2+})_{0.044}Zn_{0.956}O$ NBs are presented in Figure 5. Some remarkable features of the EPR spectrum include the following: (i) Any high-field signal at Landé factor $g = 1.96$ was observed, suggesting that an isolated neutral V_O charge state does not exist. (ii) There are two broadening EPR signals: the broad resonance signal (peak I) at $g \sim 2.0566$ close to the free-electron value ($g_e = 2.0023$) is generally attributed to an unpaired electron trapped on a V_O site (i.e., F centers or $F^+ = V_O^{2+} + e^-$),[51] and unknown peak II with a g factor close to 3–6, which is quite different from the previous EPR spectrum of Cu impurities in single-crystal ZnO.[52] (iii) Two g factors tend to increase with decreasing temperature. A possible explanation is that they are anisotropic g factors.[50] Peak I is also due to the Cu^{2+} ion ($g \sim 2.049$),[53] confirming Cu-ion substitution into Zn sites again. Deviation of the g factor from g_e and the Cu^{2+} ion ($g \sim 2.049$) is susceptible to the spin–orbit interaction $\Delta g \propto \lambda$,[50] suggesting that the Cu^{2+} ion does not freely exist where λ is the spin–orbit interaction parameter. The single ultralow-field (i.e., giant g factor) broad EPR signal (peak II) is due to exchange interaction.[54] The **g** tensor calculated from this room temperature powder spectrum indicates $g_\perp = 4.7720$ (peak II) and $g_\parallel = 2.0566$ (peak I). Because the geometry is compressed octahedral (previously confirmed by PXRD in Figure 3a and Raman in Figure 3c), following Garribba et al.,[55] the ground state in the samples is determined as the d_z^2 orbital, suggesting that the Cu^{2+} ions lie in a statically distorted octahedral coordination geometry in the compounds with a predominant d_z^2 ground state. Thus, the giant g factor means that there is strong anisotropic spin–orbit coupling or interaction between the Cu^{2+} ion and F center (i.e., forming Cu^{2+}–F^+ complexes) in

dx.doi.org/10.1021/am5001135 | ACS Appl. Mater. Interfaces 2014, 6, 4490–4497

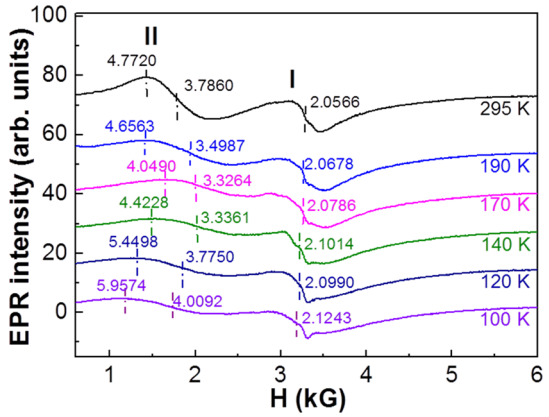

Figure 5. Temperature-dependent EPR spectra of the $(Cu_2^+/Cu_1^{2+})_{0.044}Zn_{0.956}O$ NBs. In the experiment, a Bruker ESRA-300 spectrometer operating at 9.4415 GHz (X band) between 100 K and room temperature (295 K) was used to take EPR data of the samples in a quartz capillary tube. Temperature control was maintained with a Bruker N2 temperature controller with a temperature error bar of ±1 K. The g factor can be calculated by the equation $g = h\nu/\mu_B B$, and the g values are shown.

the $(Cu_2^+/Cu_1^{2+})_{0.044}Zn_{0.956}O$ NBs. From the above analyses on microstructures and defects, the anisotropy suggests a large lattice distortion along the c-axis contribution to the 3d moment.

Furthermore, the origin of weak ferrimagnetism in the $(Cu_2^+/Cu_1^{2+})_{0.044}Zn_{0.956}O$ NBs should be attributed to F_c as well. Coey et al. reported that an electron trapped in the defect (V_O) level creates an F_c.[56] Exchange interaction between neighboring magnetic ions mediated by this F_c forms a bound magnetic polaron (BMP). Therefore, it is strongly suggested that the Cu−V_O−Cu complex can serve as singly occupied V_O denoted as F_c^+ centers to activate BMPs, giving rise to the ferromagnetic ordering component, which is due to F_c. Brant et al. reported that the Cu^{2+}−V_O complexes act as electron traps and convert to nonparamagnetic Cu^+−V_O complexes when the TiO_2 crystals are illuminated at low temperature.[57] Moreover, our previous work on Co^{2+}-doped ZnO NWs demonstrates that an F_c (=V_O^+) mechanism is proposed to explain the correlating exciton quenching and occurrence of ferrimagnetism.[6] As for the Cu^{2+} ($3d^9$) state, the Cu 3d bands are very close to the O 2p bands, near the Fermi level, enabling possible strong hybridization between O 2p and Cu 3d in the CuO_4 tetrahedron.[58] This is consistent with that of Coey et al.,[59] in which the delocalized holes induced by O 2p can be strongly hybridized with the localized unoccupied 2-fold t_2 subband of Cu 3d states to yield BMPs. Possible Cu^{2+}−V_O (accurately Cu^{2+}−V_O^+ or further Cu^{2+}−F_c) pairs form, as shown in Figure 6a, resulting from p−d hybridization between the 3d band of Cu and ZnO valence bands (O p bands) due to the substitution of Zn^{2+} in the ZnO lattice by Cu^{2+} ions[60,61] and, subsequently, the short-range Cu−O−Cu AFM superexchange[42] as one set of ferromagnetic sublattices, as shown in Figure 6b. Thus, one proposes that F_c plays an important role in Cu doping, inducing ferromagnetism-to-ferrimagnetism crossover via Cu^{2+}−F_c−Cu^{2+} pairs. Additionally, another possible explanation for the origin of ferrimagnetism is due to the larger internal strain (up to 1.98%) in the $(Cu_2^+/Cu_1^{2+})_{0.044}Zn_{0.956}O$ NBs, similar to the previous report that a larger strain can result in enhancement of RTFM.[62]

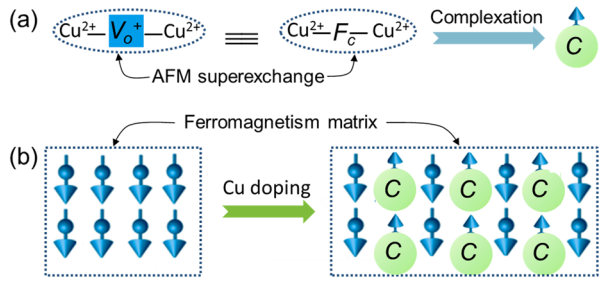

Figure 6. (a) Possible Cu^{2+}−V_O (accurately Cu^{2+}−V_O^+ or further Cu^{2+} ion−F center complexes) pair forms, where V_O^+ denotes a V_O capturing one electron, resulting from p−d hybridization between 3d band of Cu and O p bands (accurately V_O p bands). F_c and C represents the F center and the Cu^{2+} ion−F_c complex, respectively. (b) Schematic showing the Cu doping ZnO induced from the ferromagnetism-to-ferrimagnetism crossover.

4. CONCLUSION

Mixed-cation Cu^+/Cu^{2+} doping-induced novel nanoscale phenomena, including PL quenching and ferrimagnetism with $T_N \approx 14$ K, were found in as-calcined $(Cu_2^+/Cu_1^{2+})_{0.044}Zn_{0.956}O$ electrospun NBs, which is consistent with the Co^{2+}-doped ZnO case. There is high strain (up to 1.98%) and shrunken lattice distortion ($\Delta V/V_0 \sim 0.127\%$) in the $(Cu_2^+/Cu_1^{2+})_{0.044}Zn_{0.956}O$ NBs, leading to broken lattice symmetry and nonstoichiometry (i.e., V_O or accurately F centers), which could be possible origins of ferrimagnetism. The doping-related exciton quenching is found to be associated with the origin of ferrimagnetism in the $(Cu_2^+/Cu_1^{2+})_{0.044}Zn_{0.956}O$ NBs. When the results of defect-state-related PXRD (Figure 3a), Raman (Figure 3c), PL (Figure 3d), XPS (Figure 4e), and EPR (Figure 5) spectra are combined, it is suggested that complicated interactions among the high-strain, lattice-distortion F centers result in the formation of Cu^{2+} ion−F center complexes (i.e., Cu^{2+}−F^+ complexes) in the $(Cu_2^+/Cu_1^{2+})_{0.044}Zn_{0.956}O$ NBs. The study might be improving our understanding of the rich physical properties in ZnO-based DMSO NWs.

AUTHOR INFORMATION

Corresponding Author

*E-mail: phyjmli@zju.edu.cn.

Notes

The authors declare no competing financial interest.

ACKNOWLEDGMENTS

J.-M.L. acknowledges support from the National Natural Science Foundation of China (Grant 51072179), and this work is also supported by the Fundamental Research Funds for the Central Universities of China (Grant 2013FZA3003).

REFERENCES

(1) Venkatesan, M.; Fitzgerald, C. B.; Coey, J. M. D. Thin films: Unexpected Magnetism in a Dielectric Oxide. *Nature* **2004**, *430*, 630.

(2) Pearton, S. J.; Ren, F.; Wang, Y. L.; Chu, B. H.; Chen, K. H.; Chang, C. Y.; Lim, W. T.; Lin, J. S.; Norton, D. P. Recent Advances in Wide Bandgap Semiconductor Biological and Gas Sensors. *Prog. Mater. Sci.* **2010**, *55*, 1−59.

(3) Reneker, D. H.; Chun, I. Nanometre Diameter Fibres of Polymer, Produced by Electrospinning. *Nanotechnology* **1996**, *7*, 216−233.

(4) Agarwal, S.; Greiner, A.; Wendorff, J. H. Functional Materials by Electrospinning of Polymers. *Prog. Polym. Sci.* **2013**, *38*, 963−991.

(5) Li, J. M.; Zeng, X. L.; Mo, A. D.; Xu, Z. A. Fabrication of Cuprate Superconducting $La_{1.85}Sr_{0.15}CuO_4$ Nanofibers by Electrospinning and Subsequent Calcination in Oxygen. *CrystEngComm* **2011**, *13*, 6964−6967.
(6) Li, J. M.; Zeng, X. L.; Wu, G. Q.; Xu, Z. A. Exciton Quenching and Ferromagnetism-to-Ferrimagnetism Crossover in Diluted Magnetic Semiconducting $Zn_{1-x}Co_xO$ Nanogranular Nanofibers. *CrystEngComm* **2012**, *14*, 525−532.
(7) Li, J. M.; Zeng, X. L.; Dong, Y. H.; Xu, Z. A. White-Light Emission and Weak Antiferromagnetism from Cubic Rare-Earth Oxide Eu_2O_3 Electrospun Nanostructures. *CrystEngComm* **2013**, *15*, 2372−2377.
(8) Li, J. M.; Zeng, X. L.; Xu, Z. A. Partial Cationic Inversion-Induced Magnetic Hardening of Densely Packed 23-nm-Sized Nanocrystallite-Interacting Nickel Ferrite Electrospun Nanowires. *Appl. Phys. Lett.* **2013**, *103*, 232410.
(9) Li, J. M.; Wei, D. P.; Hu, Y. B.; Fang, J.; Xu, Z. A. Synthesis of Ultrafine Green-Emitting $BaCO_3$ Nanowires with 18.5 nm-Diameter by CO_2 Vapor-Assisted Electrospinning. *CrystEngComm* **2014**, *16*, 964−968.
(10) Dietl, T. Origin and Control of Ferromagnetism in Dilute Magnetic Semiconductors and Oxides. *J. Appl. Phys.* **2008**, *103*, 07D111-.
(11) Dietl, T. A Ten-Year Perspective on Dilute Magnetic Semiconductors and Oxides. *Nat. Mater.* **2010**, *9*, 965−974.
(12) Kittel, C. *Introduction to Solid State Physics*, 7th ed.; John Wiley & Sons: New York, 1996.
(13) Chen, Y. Y.; Duh, J. G.; Chiou, B. S.; Peng, C. G. Luminescent Mechanisms of ZnS:Cu:Cl and ZnS:Cu:Al Phosphors. *Thin Solid Films* **2001**, *392*, 50−55.
(14) Xu, C. X.; Sun, X. W.; Zhang, X. H.; Ke, L.; Chua, S. J. Photoluminescent Properties of Copper-Doped Zinc Oxide Nanowires. *Nanotechnology* **2004**, *15*, 856−861.
(15) Khan, Z. A.; Rai, A.; Barman, S. R.; Ghosh, S. Green Luminescence and Room Temperature Ferromagnetism in Cu Doped ZnO. *Appl. Phys. Lett.* **2013**, *102*, 022105.
(16) Huang, X. H.; Zhang, C.; Tay, C. B.; Venkatesan, T.; Chua, S. J. Green Luminescence from Cu-Doped ZnO Nanorods: Role of Zn Vacancies and Negative Thermal Quenching. *Appl. Phys. Lett.* **2013**, *102*, 111106.
(17) Shalish, I.; Temkin, H.; Narayanamurti, V. Size-Dependent Surface Luminescence in ZnO Nanowires. *Phys. Rev. B* **2004**, *69*, 245401.
(18) Chrissanthopoulos, A.; Baskoutas, S.; Bouropoulos, N.; Dracopoulos, V.; Tasis, D.; Yannopoulos, S. N. Novel ZnO Nanostructures Grown on Carbon Nanotubes by Thermal Evaporation. *Thin Solid Films* **2007**, *515*, 8524−8528.
(19) Ozgur, U.; Alivov, Y. I.; Liu, C.; Teke, A.; Reshchikov, M. A.; Doan, S.; Avrutin, V.; Cho, S. J.; Morkocu, H. A Comprehensive Review of ZnO Materials and Devices. *J. Appl. Phys.* **2005**, *98*, 041301.
(20) Gao, P.; Chen, Y. J.; Wang, Y.; Zhang, Q.; Li, X. F.; Hu, M. A Simple Recycling and Reuse Hydrothermal Route to ZnO Nanorod Arrays, Nanoribbon Bundles, Nanosheets, Nanocubes and Nanoparticles. *Chem. Commun.* **2009**, *19*, 2762−2764.
(21) Zhang, Z. Y.; Shao, C. L.; Li, X. H.; Wang, C. H.; Zhang, M. Y.; Liu, Y. C. Electrospun Nanofibers of *p*-Type NiO/*n*-Type ZnO Heterojunctions with Enhanced Photocatalytic Activity. *ACS Appl. Mater. Interfaces* **2012**, *4*, 4807−4816.
(22) Bao, D.; Gao, P.; Wang, L. Q.; Wang, Y.; Chen, Y. J.; Chen, G. R.; Li, G. B.; Chang, C.; Qin, W. ZnO Nanorod Arrays and Hollow Spheres through a Facile Room-Temperature Solution Route and Their Enhanced Ethanol Gas-Sensing Properties. *ChemPlusChem* **2013**, *78*, 1266−1272.
(23) Chakraborti, D.; Narayan, J.; Prater, J. T. Room Temperature Ferromagnetism in $Zn_{1-x}Cu_xO$ Thin Films. *Appl. Phys. Lett.* **2007**, *90*, 062504.
(24) Khan, Z. A.; Ghosh, S. Robust Room Temperature Ferromagnetism in Cu Doped ZnO Thin Films. *Appl. Phys. Lett.* **2011**, *99*, 042504.
(25) Izumi, F.; Ikeda, T. A Rietveld-Analysis Program RIETAN-98 and Its Applications to Zeolites. *Mater. Sci. Forum* **2000**, *321−324*, 198−203.
(26) Baskoutas, S.; Bester, G. Conventional Optics from Unconventional Electronics in ZnO Quantum Dots. *J. Phys. Chem. C* **2010**, *114*, 9301−9307.
(27) Li, J. M. Shrunk Lattice Structure and Interdiffusion Characteristics of 5 nm Thick Al_2O_3 Ultrathin Films Sputtered on Silicon. *Nanotechnology* **2008**, *19*, 035604.
(28) Williamson, G. K.; Hall, W. H. X-Ray Line Broadening from Filed Aluminium and Wolfram. *Acta Metall.* **1953**, *1*, 22−31.
(29) Li, J. M.; Quan, M. X.; Hu, Z. Q. Preferential Precipitation Sequence of Metastable Phase during Crystallization of $(Fe_{0.99}Mo_{0.01})_{78}Si_9B_{13}$ Metallic Glass. *Appl. Phys. Lett.* **1996**, *69*, 2356−2357.
(30) Rajalakshmi, M.; Arora, A. K.; Bendre, B. S.; Mahamuni, S. Optical Phonon Confinement in Zinc Oxide Nanoparticles. *J. Appl. Phys.* **2000**, *87*, 2445−2448.
(31) Arguello, C. A.; Rousseau, D. L.; Porto, S. P. S. First-Order Raman Effect in Wurtzite-Type Crystals. *Phys. Rev.* **1969**, *181*, 1351.
(32) Exarhos, G. J.; Rose, A.; Windisch, C. F., Jr. Spectroscopic Characterization of Processing-Induced Property Changes in Doped ZnO Films. *Thin Solid Films* **1997**, *308−309*, 56−62.
(33) Exarhos, G. J.; Sharma, S. K. Influence of Processing Variables on the Structure and Properties of ZnO Films. *Thin Solid Films* **1995**, *270*, 27−32.
(34) Li, J. M. Highly UV Luminescent ZnO Microtetrapod-on-Nanowire Hybrids. *Nanotechnology* **2010**, *21*, 175603.
(35) Li, J. M.; Zeng, X. L.; Huang, Q.; Xu, Z. A. Morphological Diversity and Alternate Evolution in Tin-Assisted Vapor-Transport-Grown ZnO Micro-Nanocrystal Tetrapods. *CrystEngComm* **2012**, *14*, 7800−7806.
(36) Li, J. M.; Dai, L. G.; Wan, X. P.; Zeng, X. L. An "Edge to Edge" Jigsaw-Puzzle Two-Dimensional Vapor-Phase Transport Growth of High-Quality Large-Area Wurtzite-Type ZnO (0001) Nanohexagons. *Appl. Phys. Lett.* **2012**, *101*, 173105.
(37) Li, J. M.; Wang, X. P.; Dai, L. G.; Xu, Z. A. Non-Layered Wurtzite-Type Extralarge-Area Flexible ZnO (01−10) Paper-Like Nanostructures Grown by Electrostatically Induced Vapor-Phase Transport. *CrystEngComm* **2013**, *15*, 1179−1184.
(38) De Lourdes Ruiz Peralta, Ma.; Pal, U.; Sánchez Zeferino, R. Photoluminescence (PL) Quenching and Enhanced Photocatalytic Activity of Au-Decorated ZnO Nanorods Fabricated through Microwave-Assisted Chemical Synthesis. *ACS Appl. Mater. Interfaces* **2012**, *4*, 4807−4816.
(39) Brumage, W. H.; Dorman, C. F.; Quade, C. R. Temperature-Dependent Paramagnetic Susceptibilities of Cu^{2+} and Co^{2+} as Dilute Impurities in ZnO. *Phys. Rev. B* **2001**, *63*, 104411.
(40) Ye, L. H.; Freeman, A. J.; Delley, B. Half-Metallic Ferromagnetism in Cu-doped ZnO: Density Functional Calculations. *Phys. Rev. B* **2006**, *73*, 033203.
(41) Getzlaff, M. *Fundamentals of Magnetism*; Springer-Verlag: Berlin, 2008.
(42) Wang, X. F.; Xu, J. B.; Cheung, W. Y.; An, J.; Ke, N. Aggregation-Based Growth and Magnetic Properties of Inhomogeneous Cu-Doped ZnO Nanocrystals. *Appl. Phys. Lett.* **2007**, *90*, 212502.
(43) Moulder, J. F.; Stickle, W. F.; Sobol, P. E.; Bomben, K. D. *Handbook of X-Ray Photoelectron Spectroscopy*; Chastain, J.; King, R. C., Jr., Eds.; Physical Electronics: Eden Prairie, MN, 1995.
(44) Jiang, P.; Prendergast, D. Experimental and Theoretical Investigation of the Electronic Structure of Cu_2O and CuO Thin Films on Cu(110) Using X-Ray Photoelectron and Absorption Spectroscopy. *J. Chem. Phys.* **2013**, *138*, 024704.
(45) Schön, G. ESCA Studies of Cu, Cu_2O and CuO. *Surf. Sci.* **1973**, *35*, 96−108.
(46) Hussain, Z.; Saim, M. A.; Khan, M. A.; Khawaja, E. E. X-ray Photoelectron and Auger-Spectroscopy Study of Copper-Sodium Germanate Glasses. *J. Non-Cryst. Solids* **1989**, *110*, 44−52.

(47) Pol, V. G.; Reisfeld, R.; Gedanken, G. A. Sonochemical Synthesis and Optical Properties of Europium Oxide Nanolayer Coated on Titania. *Chem. Mater.* **2002**, *14*, 3920−3924.
(48) Wesselinowa, J. M. Size and Anisotropy Effects on Magnetic Properties of Antiferromagnetic Nanoparticles. *J. Magn. Magn. Mater.* **2010**, *322*, 234−237.
(49) Schulman, J. H.; Compton, W. D. *Color Centers in Solids*; Pergamon: Oxford, U.K., 1962.
(50) Ikeya, M. *New Applications of Electron Spin Resonance: Dating, Dosimetry and Microscopy*; World Scientific Publishing Co. Pte. Ltd.: Singapore, 1993.
(51) Zeng, H. B.; Duan, G. T.; Li, Y.; Yang, S. K.; Xu, X. X.; Cai, W. P. Blue Luminescence of ZnO Nanoparticles Based on Non-Equilibrium Processes: Defect Origins and Emission Controls. *Adv. Funct. Mater.* **2010**, *20*, 561−572.
(52) Dietz, R. E.; Kamimura, H.; Sturge, M. D.; Yariv, A. Electronic Structure of Copper Impurities in ZnO. *Phys. Rev.* **1963**, *132*, 1559.
(53) Jagannatha Reddy, A.; Kokila, M. K.; Nagabhushana, H.; Chakradhar, R. P. S.; Shivakumara, C.; Rao, J. L.; Nagabhushana, B. M. Structural, Optical and EPR studies on ZnO:Cu Nanopowders Prepared via Low Temperature Solution Combustion Synthesis. *J. Alloys Compd.* **2011**, *509*, 5349−5355.
(54) Elilarassi, R.; Chandrasekaran, G. Structural, Optical and Magnetic Characterization of Cu-Doped ZnO Nanoparticles Synthesized Using Solid State Reaction Method. *J. Mater. Sci.: Mater. Electron* **2010**, *21*, 1168−1173.
(55) Garribba, E.; Micera, G. The Determination of the Geometry of Cu(II) Complexes: An EPR Spectroscopy Experiment. *J. Chem. Educ.* **2006**, *83*, 1229−1232.
(56) Coey, J. M. D.; Douvalis, A. P.; Fitzgerald, C. B.; Venkatesan, M. Ferromagnetism in Fe-doped SnO_2 Thin Films. *Appl. Phys. Lett.* **2004**, *84*, 1332−1334.
(57) Brant, A. T.; Yang, S.; Giles, N. C.; Zafar Iqbal, M.; Manivannan, A.; Halliburto, L. E. Oxygen Vacancies Adjacent to Cu^{2+} Ions in TiO_2 (Rutile) Crystals. *J. Appl. Phys.* **2011**, *109*, 073711.
(58) Ye, L. H.; Freeman, A. J.; Delley, B. Half-Metallic Ferromagnetism in Cu-doped ZnO: Density Functional Calculations. *Phys. Rev. B* **2006**, *73*, 033203.
(59) Coey, J. M. D.; Venkatesan, M.; Fitzgerald, C. B. Donor Impurity Band Exchange in Dilute Ferromagnetic Oxides. *Nat. Mater.* **2005**, *4*, 173−179.
(60) Tian, Y. F.; Li, Y. F.; He, M.; Ade Putra, I.; Peng, H. Y.; Yao, B.; Cheong, S. A.; Wu, T. Bound Magnetic Polarons and p−d Exchange Interaction in Ferromagnetic Insulating Cu-doped ZnO. *Appl. Phys. Lett.* **2011**, *98*, 162503.
(61) Gilliland, S. J.; Sans, J. A.; Sánchez-Royo, J. F.; Almonacid, G.; García-Domene, B.; Segura, A.; Tobias, G.; Canadell, E. Role of p−d and s−d Interactions in the Electronic Structure and Band Gap of $Zn_{1-x}M_xO$ (M = Cr, Mn, Fe, Co, Ni, and Cu): Photoelectron and Optical Spectroscopy and First-Principles Band Structure Calculations. *Phys. Rev. B* **2012**, *86*, 155203.
(62) Liu, X. J.; Song, C.; Zeng, F.; Pan, F.; He, B.; Yan, W. S. Strain-Induced Ferromagnetism Enhancement in Co: ZnO Films. *J. Appl. Phys.* **2008**, *103*, 093911.